Bai, H. and B.G. Thomas, "Two Phase Flow in Tundish Nozzles During Continuous Casting of Steel", Materials Processing in the Computer Age III, V. Voller and H. Henein, eds., TMS Annual Meeting, Nashville, TN, March 12-16, 2000, pp. 85-99.

TWO-PHASE FLOW IN TUNDISH NOZZLES DURING CONTINUOUS CASTING OF STEEL

H. Bai and B. G. Thomas

Department of Mechanical and Industrial Engineering
University of Illinois at Urbana-Champaign
1206 West Green Street, Urbana, IL 61801
Ph: 217-333-6919; Fax: 217-244-6534
email: h-bai@uiuc.edu; bgthomas@uiuc.edu

Abstract

A three-dimensional finite difference model has been developed to study the liquid steel-argon bubble two-phase turbulent flow in continuous casting tundish nozzles. Experiments have been performed on a 0.4-scale water model to verify the computational model by comparing its prediction with velocity measurements using PIV (Particle Image Velocimetry) technology. The computational model was developed using CFX and then employed to investigate the effects of various casting process variables. A fast, simple inverse model to quantify relationships between those process variables was developed, based on interpolation of the numerical model results, using Bernoulli's Equation and advanced multivariable curve fitting methods. Predictions using this model compare well with plant measurements. The model has been applied to present trends and observations on the relationship between casting speed, tundish depth, slide gate opening, and argon gas injection rate. The results can also be used to predict the theoretical steel flow rate through the nozzle, so that clogging conditions can be identified in the plant.

Introduction

Tundish nozzle geometry is one of the few variables that are both very influential on the casting process and relatively inexpensive to change. Designing an effective nozzle requires quantitative knowledge of the relationship between nozzle geometry and other process variables on the influential characteristics of the flow exiting the nozzle. This relationship depends on the flow pattern within the nozzle components. Most previous modeling studies of flow in the nozzle have focused on single-phase flow [1-4]. Argon injection into nozzle is an efficient and widely employed method to reduce nozzle clogging, even though the real working mechanism(s) are still not fully understood [5]. Argon injection may greatly affect the flow pattern in the nozzle, and subsequently in the mold. Therefore, two-phase flow modeling is needed to improve understanding of fluid flow in the nozzle.

In this paper, a three-dimensional finite difference model is developed to study the liquid steel-argon bubble two-phase turbulent flow in the slide-gate tundish nozzles of continuous casting process. Experiments have been performed on a 0.4-scale water model at LTV Steel to verify the model by comparing the model predictions with velocity measurements using Particle Image Velocimetry. The validated model is then employed to investigate the effects of various casting process variables and the complex relationship between them.

Model Formulation

Governing Equations

The liquid steel flows from a tundish, through a slide-gate nozzle where it mixes with argon bubbles injected through the nozzle wall, and jets through bifurcated ports into a continuous casting mold. The flow is inherently three-dimensional, two-phase and highly turbulent. The Reynolds number, based on the nozzle bore diameter (D), is typically of the order of 10^5. The multiphase model solves the steady-state mass and momentum conservation equations for incompressible Newtonian fluids where each phase has its own set of continuity and momentum equations. Coupling is achieved through inter-phase drag between liquid steel and argon bubbles. The governing equations for the liquid phase are:

$$\frac{\partial\left[(v_l)_i f_l\right]}{\partial x_i} = 0 \tag{1}$$

$$\rho_l \frac{\partial\left[(v_l)_j (v_l)_i f_l\right]}{\partial x_j} = -f_l \frac{\partial p_l}{\partial x_i} + \frac{\partial}{\partial x_j}\left[f_l(\mu_l + \mu_t)\left(\frac{\partial (v_l)_i}{\partial x_j} + \frac{\partial (v_l)_j}{\partial x_i} \right)\right] + f_l \rho_l g_i + c_{l,g}\left[(v_g)_i - (v_l)_i\right] \tag{2}$$

and for the gas phase are:

$$\frac{\partial\left[(v_g)_i f_g\right]}{\partial x_i} = 0 \tag{3}$$

$$\rho_g \frac{\partial\left[(v_g)_j (v_g)_i f_g\right]}{\partial x_j} = -f_g \frac{\partial p_g}{\partial x_i} + \frac{\partial}{\partial x_j}\left[f_g \mu_g \left(\frac{\partial (v_g)_i}{\partial x_j} + \frac{\partial (v_g)_j}{\partial x_i} \right)\right] + f_g \rho_g g_i + c_{l,g}\left[(v_l)_i - (v_g)_i\right] \tag{4}$$

where the indices i and j = 1,2,3 represent the x, y and z directions, $v_i = \{u, v, w\}$, subscript l donates the liquid phase and subscript g the gas phase, f is volume fraction, ρ is density, μ is molecular viscosity and μ_t is the turbulent (or eddy) viscosity. Repeated indices imply summation. Because the density of the gas is 3~4 orders of magnitude smaller than that of the liquid, turbulence in the gas phase is neglected. The standard, two-equation K-ε turbulence model is chosen for the liquid phase, which requires the solution of two additional transport equations to find the turbulent kinetic energy, K, and the turbulent dissipation, ε, fields [6],

$$\rho_l \frac{\partial\left((v_l)_j K\right)}{\partial x_j} = \frac{\partial}{\partial x_j}\left(\frac{\mu_l}{\sigma_k}\frac{\partial K}{\partial x_j}\right) + \mu_l \frac{\partial v_j}{\partial x_i}\left(\frac{\partial v_i}{\partial x_j} + \frac{\partial v_j}{\partial x_i}\right) - \rho_l \varepsilon \tag{5}$$

$$\rho_l \frac{\partial\left((v_l)_j \varepsilon\right)}{\partial x_j} = \frac{\partial}{\partial x_j}\left(\frac{\mu_l}{\sigma_\varepsilon}\frac{\partial \varepsilon}{\partial x_j}\right) + C_1 \frac{\varepsilon}{K}\mu_l \frac{\partial v_j}{\partial x_i}\left(\frac{\partial v_i}{\partial x_j} + \frac{\partial v_j}{\partial x_i}\right) - C_2 \rho_l \frac{\varepsilon^2}{K} \tag{6}$$

The turbulent viscosity μ_t is calculated from the turbulent kinetic energy and dissipation by

$$\mu_t = C_\mu \rho_l \frac{K^2}{\varepsilon} \tag{7}$$

The above equations contain five empirical constants that appear to produce reasonable behavior for a wide range of flow [7] when given standard values as follows:

$$C_1 = 1.44,\ C_2 = 1.92,\ C_\mu = 0.09,\ \sigma_K = 1.00,\ \sigma_\varepsilon = 1.30$$

There is an obvious constraint that the volume fractions sum to unity:

$$f_l + f_g = 1 \tag{8}$$

Equation (1) to (8) represent 12 equations with 13 unknowns (*u, v, w, p, f for each phase, and* μ_t*, K,* ε for liquid turbulence). The final equation needed to close the system is given by an algebraic constraint on the pressure. The simple assumption was made that both phases share the same pressure field:

$$p_l = p_g = p \tag{9}$$

The last term of momentum equation (2) and (4) describes inter-phase transfer of momentum between the liquid steel and the argon bubbles. Here, $c_{l,g}$ denotes the inter-phase momentum exchange coefficient, which is related to the relative velocity of the two phases by

$$c_{l,g} = \frac{3}{4}\frac{C_D}{D} f_g \rho_l \left|(v_l)_i - (v_g)_i\right| \tag{10}$$

where D is the bubble diameter. The non-dimensional drag coefficient C_D is a function of the bubble Reynolds number, defined as Re_{bub}

$$Re_{bub} = \frac{\rho_l \left|v_l - v_g\right| D}{\mu_l} \tag{11}$$

The function $C_D(Re_{bub})$ may be determined experimentally, and is known as the drag curve. The drag curve for bubbles can be correlated in several distinct regions:

1) Stokes regime, $0 \le Re_{bub} \le 0.2$

$$C_D = \frac{24}{Re_{bub}} \tag{12}$$

2) Allen regime, $0 \le Re_{bub} \le 500 \sim 1000$,

$$C_D = \frac{24}{Re_{bub}}\left(1 + 0.15 Re_{bub}^{\ 0.687}\right) \tag{13}$$

3) Newton regime, $500 \sim 1000 \le Re_{bub} \le 1 \sim 2\text{x}10^5$,

$$C_D = 0.44 \quad (14)$$

4) Super-critical regime, $Re_{bub} > 1\sim2\text{x}10^5$,

$$C_D = 0.1 \quad (15)$$

Analysis of the results revealed that most bubbles in this study are in the Stokes regime, with a few in the Allen regime. The governing equations (1~8) are discretized using the finite difference method and solved with the CFX code version 4.2 developed by AEA Technology [8].

Computational domain and boundary conditions

Figure 1 shows the outline of the computational domain geometry of the slide-gate nozzle, its boundary condition settings and main dimensions. The top of the nozzle, or the liquid inlet, is specified as the fixed liquid velocity corresponding to the chosen constant flow rate. Specifically, the average velocity of the liquid at the top was derived from the knowledge of the casting speed and the mold cross-section size. A uniform normal velocity profile was assumed, which is a reasonable approximation of the 1/7 power-law turbulent profile expected in pipe flow. Turbulent kinetic energy and turbulent dissipation are also specified at the inlet to the nozzle. They take the average values of the profiles calculated from a mixing-length model for turbulent pipe flow [3]. The volume fraction of the liquid steel is unity at the top boundary.

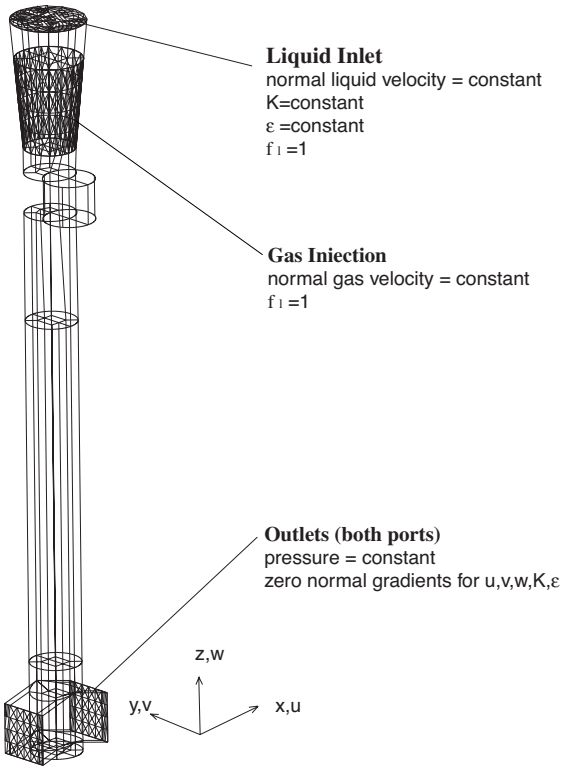

Main Dimensions and simulation conditions

SEN bore diameter	78 mm
Port width x height	78x78 mm x mm
Port thickness	30 mm
Port angle	15° down
Recessed bottom design well depth	12 mm
UTN top diameter	114 mm
UTN length	241.5 mm
Slide-gate thickness	63 mm
Slide-gate diameter	78 mm
Total length	1152.5 mm
Gate orientation	90°
SEN submerged depth	200 mm
Average bubble diameter	1 mm
Molecular viscosity of the liquid steel	5.6E-3 kg/m-s
Molecular viscosity of the argon gas	7.4E-5 kg/m-s
Density of the liquid steel	7021 kg/m^3
Density of the argon gas	0.559 kg/m^3

Figure 1 - Computational domain, boundary conditions, main dimensions and simulation conditions of the standard slide-gate nozzle

The gas injection region, on the surface of the upper tundish nozzle (UTN) wall, is specified as a fixed velocity boundary for the gas phase. The fixed normal velocity for the gas phase is the gas injection flow rate through that region divided by the region area. It should be noted that the argon gas flow rate used in modeling is always the "hot" argon flow rate, which is about 5 times greater than the "cold" flow rate, as discussed further in the section on simulation conditions.

Fixed pressure boundary conditions are specified at the outlet, or the ports of the nozzle. The specified pressure is set to the hydrostatic pressure (which depends on the SEN submergence depth), which is reasonably close to the actual pressure at the nozzle ports. Zero normal gradients

are set for all transported variables (u, v, w, K, ε). This treatment of the outlet has proven to be an acceptable approximation for the conditions at the nozzle ports in previous works on single-phase flow [1-4].

Model Validation

Water model experiments and PIV measurements

Flow visualization and velocity measurements were made using 0.4-scale water models of the tundish, nozzle and mold of the caster at LTV Steel (Cleveland, OH). The nozzle geometry, shown in Table I, was slightly different from the standard conditions used in the parametric study, shown in Figure 1. The PIV (Particle Image Velocimetry) system developed by DANTEC Measurement Technology was used to measure the velocity field at the plane of interest near the nozzle port. PIV is a planar measurement technology wherein a pulsed laser light sheet is used to illuminate a flow field seeded with tracer particles small enough to accurately follow the flow. The positions of the particles are recorded with a digital CCD (Charged Coupled Device) camera at each instant the light sheet is pulsed. The images from two neighboring pulses of the light sheet are processed to match up individual particles and calculate the vector displacement of each. Knowledge of the time interval between the two light sheet pulses then permits the computation of the flow velocity over the brief time interval, or "exposure", and the flow velocities thus obtained comprise an instantaneous velocity field. In this work, the time between pulses in each exposure was 1.5 ms and the time between the two neighboring exposures was 0.533 second. To obtain the time-averaged or "steady" velocity field, the results from 50 exposures averaged. Errors in matching up particles sometimes produce abnormal huge velocities at a single point, which are easy to recognize. Thus, before averaging, the vector plot of each exposure is examined and each abnormal vector is replaced by the average of its four normal neighbors. If the abnormal vector is at the nozzle port, only the neighbors on the outside of the nozzle port are averaged to obtain the replacement vector, because velocities inside the nozzle cannot be accurately measured.

Table I Nozzle dimensions and operation conditions for the PIV water experiments

Dimension/Condition	0.4 scale	Corresponding full scale
Bore (SEN) diameter	32 mm	80 mm
Port width x height	31mm x 32mm	75mm x 78mm
Port thickness	11 mm	27.5 mm
Port angle, lower edge	15˚ down	15˚ down
Port angle, upper edge	40˚ down	40˚ down
Recessed bottom well depth	4.8 mm	12 mm
UTN diameter	28 mm	70 mm
Slide-gate diameter	28 mm	70 mm
Slide-gate thickness	18 mm	45 mm
Nozzle length - total	510 mm	1275 mm
Slide-gate orientation	90°	90°
SEN submergence depth	80 mm	200 mm
Slide-gate opening (FL)	52%	52%
Liquid flow rate at inlet	7.07×10^{-4} m^3/s	1.042×10^{-2} m^3/s
Gas injection volume fraction	5.8%	5.8%
Tundish bath depth	400~410 mm	1000~1025 mm

Flow pattern observations

Flow patterns observed in the experiments can be directly compared to the numerical simulation with the model described above under the same operation conditions. Close agreement between the experiments and the numerical model was achieved. In both the water experiments and model predictions, three main recirculation zones are observed in the slide-gate nozzle: in the cavity of the middle gate plate, below the throttling gate plate, and at the nozzle ports. High gas

concentration collects in these recirculation zones. Figure 2 shows an example of the predicted

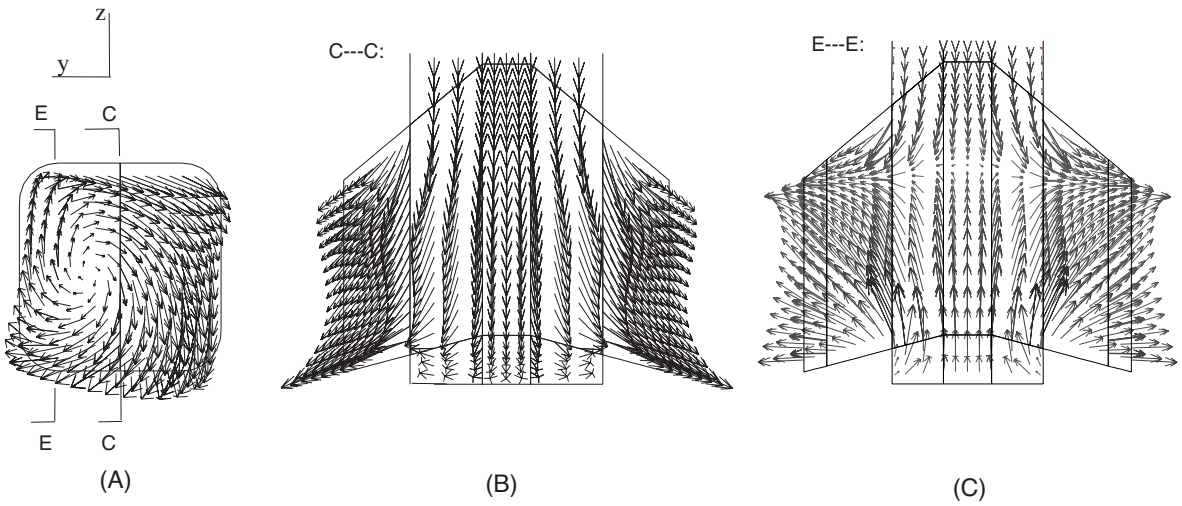

Figure 2 - Flow pattern predicted at the SEN ports for the experimental nozzle: (A) end view from the left port, (B) center-plane parallel to the wide face, (C) 12 mm from center-plane, parallel to the wide face

flow pattern near the nozzle ports. In both the simulation and the water experiments, the jet exits the ports with a single strong vortex or swirl. The vortex rotational direction is relatively stable with clockwise direction in a side view (y-z plane) at the plane of the port exit, looking directly into the left port (Figure 2A). The jet is directed approximately 29° down, as seen in the photograph of Figure 3. This is very close to the value of 27.8° down calculated from the simulation results using a weighted-average method over all nodes on the port plane [9].

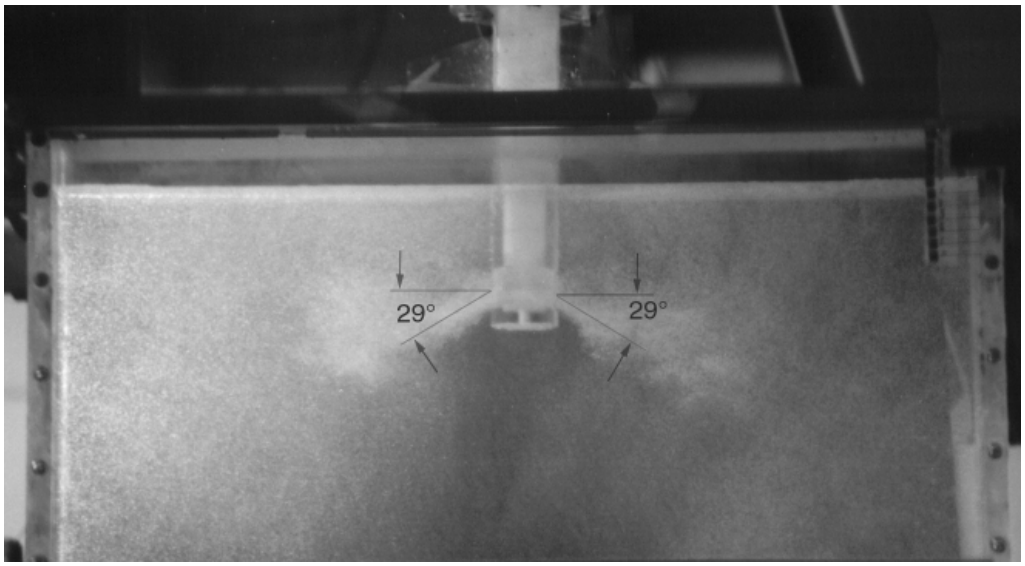

Figure 3 - Flow pattern and the average jet angle measurement in water model experiment

No obvious "back-flow" at the nozzle port was observed during the experiments. This matches the numerical computation, which predicts only outward flow at the nozzle ports, as shown in Figure 2. It is noted that the observation of no back-flow differs from many previous findings for typical nozzles [2, 4, 10]. The zero back-flow-zone in the experiments is mainly due to the special design of the SEN ports of this nozzle, which had a much steeper angle of the upper port edges (40°down) than the lower port edges (15°down) [11].

Velocity Comparisons

A quantitative comparison between the PIV measurements and the simulation results is made on the jet at the nozzle port exit. Unfortunately, the flow field inside the plastic nozzle could not be reliably measured, due to the curvature of the nozzle wall and partial opacity from the machining

cut. Figure 4(A) shows a vector plot of the PIV-measured flow field around the nozzle port in the plane parallel to the wide face of the mold. The predicted flow vector plots (B) are plotted side by side for direct visual comparison. The magnitudes of the liquid velocity at the port for measurements and prediction are then extracted and plotted together in (C). Since the PIV is a planar measurement which does not include v-component of the velocity (y-direction, perpendicular to the paper), the velocity magnitude is calculated using only the u- and w- velocity components. The "overall jet angle", defined as the weighted-average over the whole 3-D jet [9], should not be compared with the 2-D jet angle calculated from a single slice of the PIV measurements, or "slice jet angle". The slice jet angle is a simple arithmetic average of the jet angles for all measuring points (PIV) or computational cells (CFX) at the slice of the nozzle port. The time-averaged values of the "slice jet angle" are marked on Figure 4 (C).

The upper part of Figure 4 is for the slice through the nozzle center-plane (y=0), and the lower part for the slice that is away from and parallel to the center-plane (at y=12mm). The match of the velocity magnitude and the slice jet angle between the PIV measurement and the model prediction

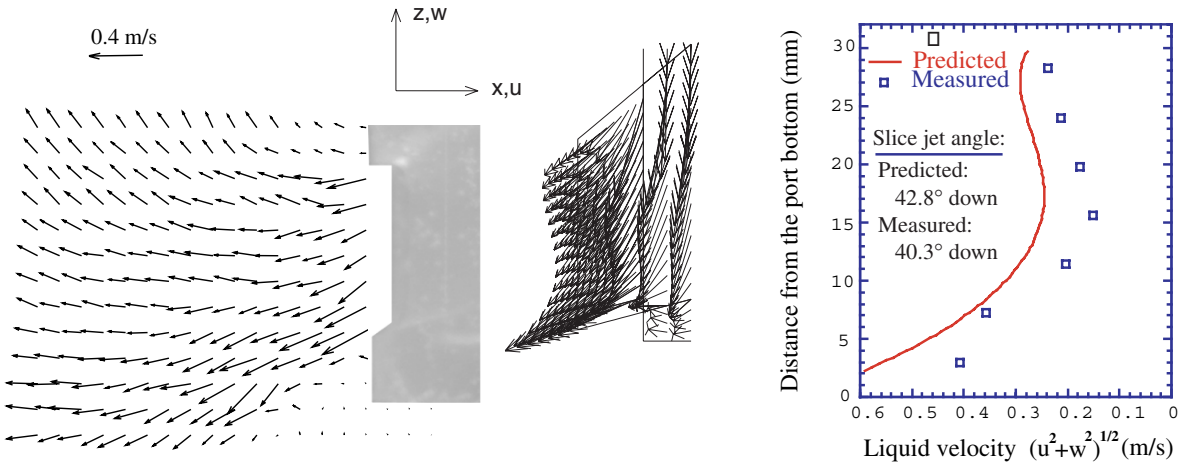

Slice (y=0) at the center-plane of the nozzle, parallel to the wide face of the mold

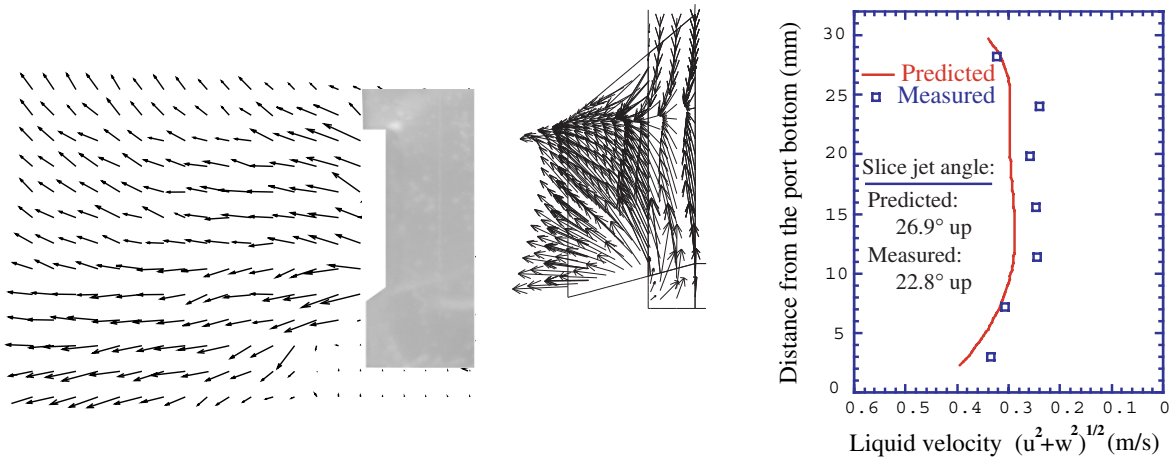

Slice (y=12mm) away from the center-plane of the nozzle, parallel to the wide face of the mold

(A) PIV measurements **(B) CFX prediction** **(C) Magnitute comparison of PIV measurements and CFX prediction**

Figure 4 – Comparison of PIV measurements and model prediction

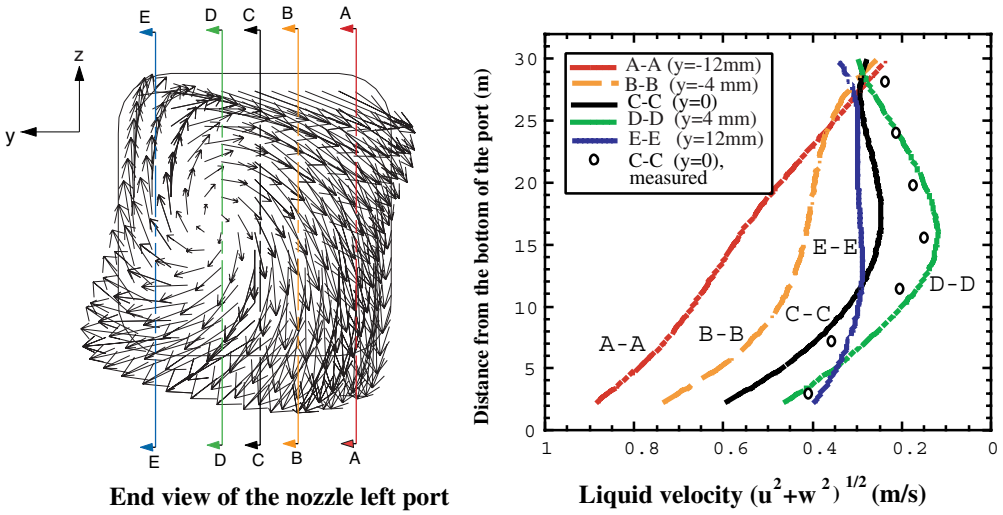

Figure 5 – Velocity profile at different vertical slices of the nozzle port

is satisfactory except that the velocity predictions are consistently slightly larger than the measurements. This is likely due to fact that the location of the pulsed laser light sheet was manually adjusted by naked eye during the PIV experiments, and thus might not lie exactly in the desired position. Figure 5 shows how the velocity magnitude might change with the slice location due to the 3-D effect of the jet vortex. It is interesting to notice the flow vector plot at the slice away from the center-plane (lower part of Figure 4). The jet in this slice is upward even though the overall jet is downward. This is consistent with the 3-D swirl of the jet discussed earlier.

Effect of Casting Operation Conditions

The validated two-phase numerical model was next employed to investigate the effects of various variables on the flow pattern and important output variables. These variables may include nozzle geometry and process variables such as casting speed, argon injection flow rate, slide-gate opening and tundish bath depth. The effects of the geometric parameters of the nozzle such as the port angle, port height, port width, port thickness, port sharp and bottom design on flow pattern in nozzle as well as on jet characteristics were extensively studied previously with the single-phase finite element model in previous work [4]. This paper will focus on the effects of the casting process variables.

Simulation conditions

The standard nozzle used in this study (shown in Figure 1) has a 90° orientation slide-gate, in which the slide-gate moves in a direction perpendicular to the wide face of the mold. Thus, the right and left sides of the mold are symmetrical. This orientation has the least bias flow between the two ports, so is widely adopted in practice. The effect of different orientations of the slide-gate has been studied elsewhere [9].

Table II - Casting Operation Conditions in Numerical Simulation

Process Variable	Symbol	Unit	Value	Notes
Casting Speed	V_C	m/min	0.2, 0.5, 1, 1.5, 2.0, 2.3	For 8"x52" slab
Gate Opening	F_L	%	40, 50, 60, 70, 100	Linear opening
Argon Flow Rate	Q_G	SPLM	0, 5, 10	"cold" argon

The casting operation conditions used in this parametric study are listed in Table II. Casting speed V_C refers to a typical size of the continuous casting steel slab (8"x52") and can be easily converted into liquid steel flow rate through the nozzle or casting speed of a different sized-slab. Gate 0pening F_L is linear fraction of the opening, defined as the ratio of the displacement of the throttling plate to the bore diameter of the SEN, and can be converted to any plant definition of gate opening, usually defined as the relative displacement to a reference position. Calculation [9] shows that argon gas has been heated (when injected through the "hot" nozzle wall) up to 99% of the molten steel temperature even before it hits the liquid steel. The argon flow rate used in the numerical model should be the "hot" argon flow rate. This is simply the product of the "cold"

argon flow rate, measured at standard conditions (STP of 25˚C and 1 atmosphere pressure) and the coefficient of gas volume expansion due to the temperature and pressure change [9], which is about 5 [12]. For convenience, the equivalent "cold" argon flow rate, which is usually monitored in the steel plant, will be used in following discussions. All of the 90 (6x5x3) different cases in Table II were simulated with the computational model, in order to perform a full parametric study on casting speed, gate opening, and argon flow rate.

Inverse model for multiple process variable relationships

For a given nozzle geometry and clogging status, the four basic casting process variables of casting speed, argon injection flow rate, gate opening and tundish bath depth are related. Choosing values for any three variables intrinsically determines the fourth. During a stable casting process, tundish bath depth and argon injection are usually kept at constant level. Gate opening is regulated to compensate for any unwanted effects, such as nozzle clogging and changes in tundish bath depth, in order to ensure a constant stable casting speed.

In numerical simulation of fluid flow in nozzle, the gate opening is incorporated into the computational domain (mesh generation), and casting speed and argon injection flow rate are implemented as inlet boundary conditions at the top inlet and gas injection region of the nozzle. For each simulation, the numerical model calculates the flow pattern as well as the pressure distribution, including the pressure-drop across the nozzle, Δp. The corresponding tundish bath depth, H_T, can be obtained from Δp by applying a simple relation based on Bernoulli's Equation, as described next and illustrated in the schematic of the process given in Figure 6.

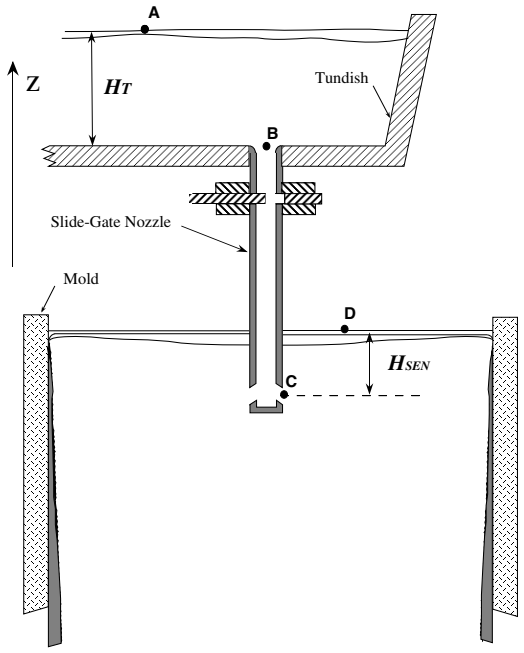

Figure 6 - Schematic of the continuous casting process showing tundish, slide-gate nozzle, mold and Location A, B, C, and D

Apply Bernoulli's Equation on location A and B:

$$p_A + \tfrac{1}{2}\rho_l U_A^2 + \rho_l g z_A = p_B + \tfrac{1}{2}\rho_l U_B^2 + \rho_l g z_B \tag{16}$$

where p and U are the pressure and velocity at these locations. Inserting $H_T = z_A - z_B$, $P_A = 0$ and $U_A \approx 0$ yields

$$H_T = \frac{p_B + \tfrac{1}{2}\rho_l U_B^2}{\rho_l g} \tag{17}$$

Apply Bernoulli's Equation on location C and D:

$$p_C + \tfrac{1}{2}\rho_l U_C^2 + \rho_l g z_C = p_D + \tfrac{1}{2}\rho_l U_D^2 + \rho_l g z_D \tag{18}$$

Since $H_{SEN} = z_D - z_C$, $P_D = 0$ and $U_D \approx 0$, then,

$$p_C = \rho_l g H_{SEN} - \tfrac{1}{2}\rho_l U_C^2 \tag{19}$$

and

$$\Delta p = p_B - p_C \tag{20}$$

Combining Equation (17), (19) and (20) gives

$$H_T = \frac{\Delta p + \rho_l g H_{SEN} + \tfrac{1}{2}\rho_l (U_B^2 - U_C^2)}{\rho_l g} \tag{21}$$

where Δp is the simulated pressure-drop, H_{SEN} is the SEN submerged depth, U_B is the average velocity at the top inlet of the nozzle and U_C is the average jet velocity at the nozzle port.

The calculated tundish bath depths (H_T) are plotted as a function of the other process variables, in Figures 7(A), (B) and (C). Each point in these plots represents one simulation case. These plots are inconvenient to apply in practice because tundish bath depth is generally an independent variable, contrary to the model formulation and results in these three plots. In order to determine and present the results in a more practical manner, an inverse model was developed in order to capture the results in a flexible manner such that any arbitrary choice of dependent variable is possible.

The first step in development of this model was to fit the points in Figures 7(A)-(C) using a multiple-variable curve fitting procedure. The lines in Figure 7 are produced with this model, which is briefly described below.

As shown in Figure 7(A), the H_T vs. V_C data fits well with a second order polynomial function, and data shown in Figure 7(B), (H_T vs. Q_G), fits well with a simple linear function. Unfortunately, a single simple function could not be found to fit the data (H_T vs. F_L) over the whole F_L range. Thus, the H_T vs. F_L data was split into two regions, with a second order polynomial function for region $F_L \leq 60\%$ and a linear function for region $F_L \geq 60\%$, as shown in Figure 7(C). The overall relationship can be written as

$$H_T = \left(a_1 V_C^2 + a_2 V_C + a_3\right)\left(a_4 F_L^2 + a_5 F_L + a_6\right)\left(a_7 Q_G + a_8\right) \qquad \text{for} \quad F_L \leq 60\% \tag{22a}$$

$$H_T = \left(a_9 V_C^2 + a_{10} V_C + a_{11}\right)\left(a_{12} F_L + a_{13}\right)\left(a_{14} Q_G + a_{15}\right) \qquad \text{for} \quad F_L \geq 60\% \tag{22b}$$

where the a_i (i=1-15) are constants. Expanding this equation yields a new pair of equations with a total of 18 and 12 unknowns respectively.

$$\begin{aligned} H_T = {} & c_1 + c_2 V_C + c_3 F_L + c_4 Q_G + c_5 V_C F_L + c_6 V_C Q_G + c_7 F_L Q_G + c_8 V_C F_L Q_G + c_9 V_C^2 + c_{10} F_L^2 \\ & + c_{11} V_C F_L^2 + c_{12} V_C^2 F_L + c_{13} V_C^2 Q_G + c_{14} F_L^2 Q_G + c_{15} V_C^2 F_L^2 + c_{16} V_C F_L^2 Q_G \\ & + c_{17} V_C^2 F_L Q_G + c_{18} V_C^2 F_L^2 Q_G \qquad \text{for} \quad F_L \leq 60\% \end{aligned} \tag{23a}$$

$$\begin{aligned} H_T = {} & c_{19} + c_{20} V_C + c_{21} F_L + c_{22} Q_G + c_{23} V_C F_L + c_{24} V_C Q_G + c_{25} F_L Q_G + c_{26} V_C F_L Q_G + c_{27} V_C^2 \\ & + c_{28} V_C^2 F_L + c_{29} V_C^2 Q_G + c_{30} V_C^2 F_L Q_G \qquad \text{for} \quad F_L \geq 60\% \end{aligned} \tag{23b}$$

where c_i (i=1,2,…,30) are all constants. To solve for the 30 constants, 30 equations are needed. Because far more than 30 data sets were simulated (Table II), a least square curve fitting technique was used to find c_i values that minimize the distance of each data point from its fitting curve [11]. The close match in Figures 7(A-C) between the lines from Equation (23) and some of the points from the computational model indicates the accuracy of this fit.

After constants c_i are known, the relatively simple Equation (23) can be inverted into equations that have either V_C, Q_G, or F_L as the dependent variable (instead of H_T). This simple "inverse model" for multiple process variable relationships can then be used to study how the process variables are related to each other. The results in Figure 7(D-E) are plotted using this model.

Theoretical steel flow rate

One direct use of the inverse model based on Equation (23) is to predict the theoretical steel flow rate through the nozzle at specific operation conditions (knowing tundish bath depth, gate opening, and argon injection flow rate). Since all simulation cases in Table II are for a non-clogged nozzle, clogging condition can be known by comparing the measured steel flow rate to the calculated theoretical steel flow rate under the same operation conditions. A clogging index may be defined as the ratio of the measured steel flow rate to the predicted theoretical steel flow rate under the same operation conditions.

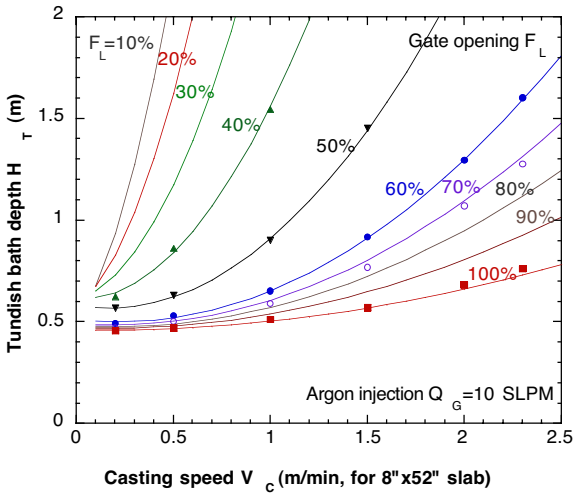

(A) H_T vs. V_C at different F_L and Q_G =10SLPM
CFX data (points) and Eq. 23 (lines)

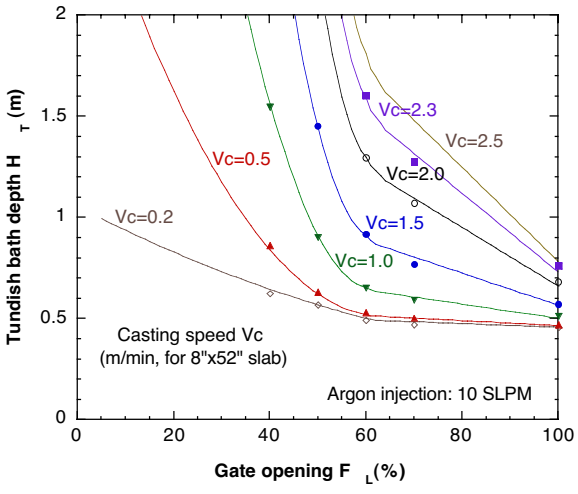

(B) H_T vs. F_L at different V_C and Q_G =10SLPM
CFX data (points) and Eq. 23 (lines)

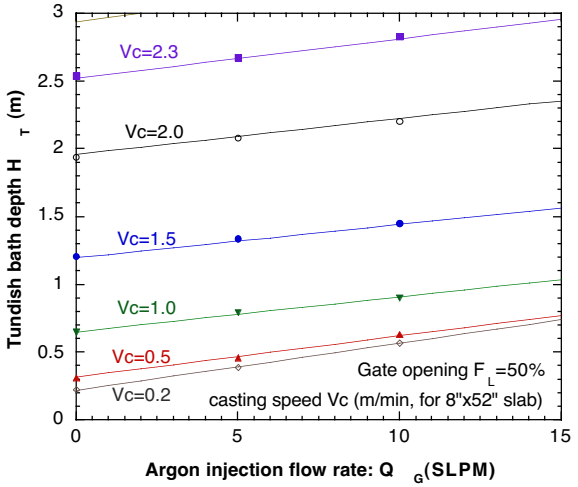

(C) H_T vs. Q_G at different V_C and F_L=50%
CFX data (points) and Eq. 23 (lines)

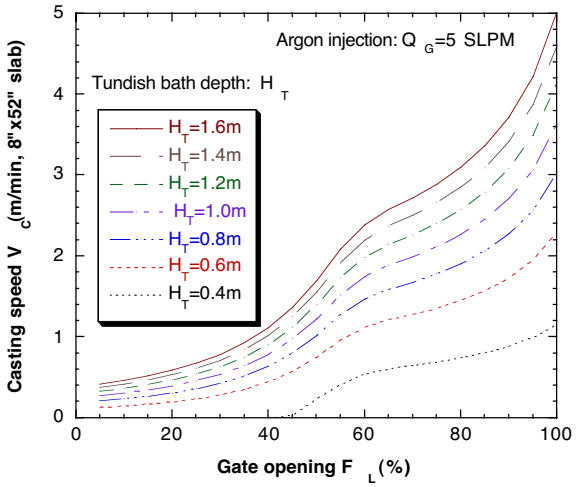

(D) V_C vs. F_L at different H_T and Q_G =5SLPM
(Inverse model)

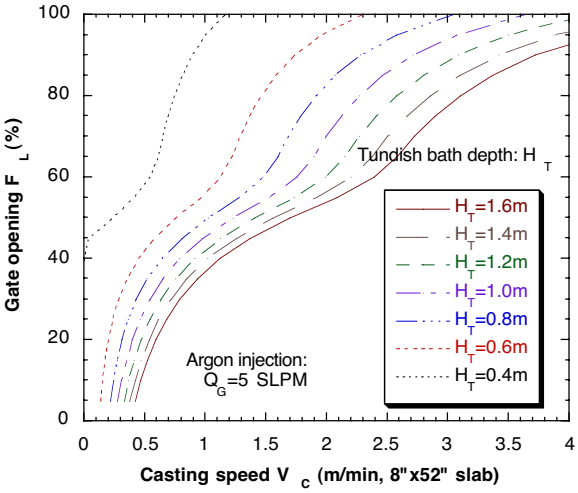

(E) F_L vs. V_C at different H_T and Q_G =5SLPM

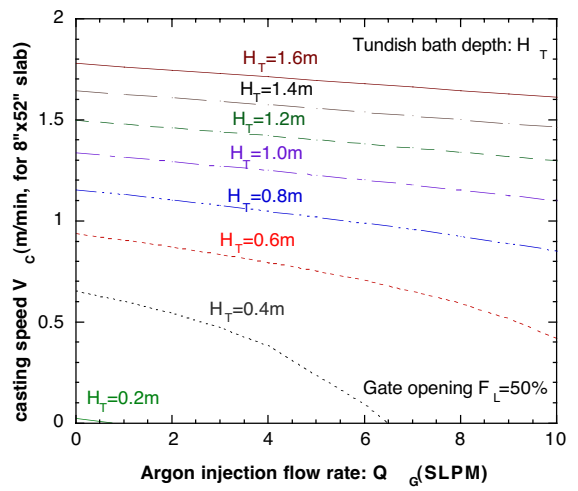

(F) V_C vs. Q_G at different H_T and F_L =50%

Figure 7 – Relationship plots of the continuous casting process variables (Tundish bath depth H_T, Casting speed V_C, Gate opening F_L and Argon injection flow rate Q_G). All lines are from relationship model and the points are from the CFX simulation output

For the example of fixed tundish bath depth (H_T), fixed gate opening (F_L) less than 60%, and fixed argon injection flow rate (Q_G), Equation (23) can be rewritten as:

$$aV_C^2 + bV_C + c = 0 \tag{24}$$

where

$$a = c_9 + c_{12}F_L + c_{13}Q_G + c_{15}F_L^2 + c_{17}F_LQ_G + c_{18}F_L^2Q_G \tag{25a}$$

$$b = c_2 + c_5F_L + c_6Q_G + c_{11}F_L^2 + c_8F_LQ_G + c_{16}F_L^2Q_G \tag{25b}$$

$$c = c_1 + c_3F_L + c_4Q_G + c_{10}F_L^2 + c_7F_LQ_G + c_{14}F_L^2Q_G - H_T \tag{25c}$$

The theoretical casting speed is then obtained from:

$$V_C = \frac{-b + \sqrt{b^2 - 4ac}}{2a} \qquad \text{for} \quad F_L \le 60\% \tag{26}$$

The other root is always negative, which is physically incorrect. Similar equations can be derived for gate openings greater than 60% and for F_L or Q_G as the dependent variable.

The theoretical steel flow rate is the product of the calculated theoretical casting speed from Equation (26) and the slab section area (8"x52"). Figure 7(D) shows a graphical representation of the inverse model given by Equation (26).

Relationship between gate opening and steel throughput

Another practical use of the inverse models based on the multiple process variable relationships in Equation (23) is to predict how gate opening changes with casting speed (or steel throughput) under specific tundish bath depth and argon flow rate. In Figure 8, another inverted form of Equation (23) was applied to make this prediction for conditions where measurements were available for comparison. Specifically, gate openings were recorded for different steel throughputs for several months at Inland Steel [13], yielding several thousand data points. Only first heats in a sequence were recorded in order to minimize the effect of clogging. The tundish bath depth was kept as a constant (H_T=1.125m) for these data, and the argon injection ranged from 7 to 10 SLPM. The nozzle geometry used in this plant study is not the same as that of the standard nozzle that Eq. 23 is based on, but it is reasonably close. The main dimensions and operation conditions used for Figure 8 are compared in Table III. The inverse model predictions required conversion of F_L to the plant definition of gate opening F_P and casting speed (m/min) to steel throughput Q_{Fe} (metric-tons/min) by

$$F_P = (1 - 24\%)F_L + 24\% \tag{27}$$

and

$$Q_{Fe} = 1.8788\ Vc \tag{28}$$

Table III – Dimensions and operation conditions for the standard and Inland nozzles

Condition/Geometry	**Standard Nozzle**	**Inland Nozzle**
Bath depth	1125 mm	1125 mm
SEN submerged depth	200 mm	120~220 mm
SEN bore	78 mm	91~96 mm
Gate diameter	78 mm	75 mm
Gate thickness	63 mm	45 mm
Port angle	15° down	35° down
Port shape	78mm x 78mm	75mm x 75mm
UTN bore	78~114 mm	80~115 mm
Nozzle total length	1152.5 mm	1123 mm
Argon injection	10 SLPM	7~10 SLPM

In addition to the inverse model, additional CFX simulations were performed for the conditions of the Inland nozzle in Table III and the results are shown in Figure 8 as 3 big dots.

Figure 8 shows that these CFX results are very close to the prediction with the inverse model, despite the slight difference in nozzle geometry. In addition to validating both models, this suggests that the inverse model derived from the standard nozzle is applicable to other practical conditions, as long as the nozzle geometry is reasonably close.

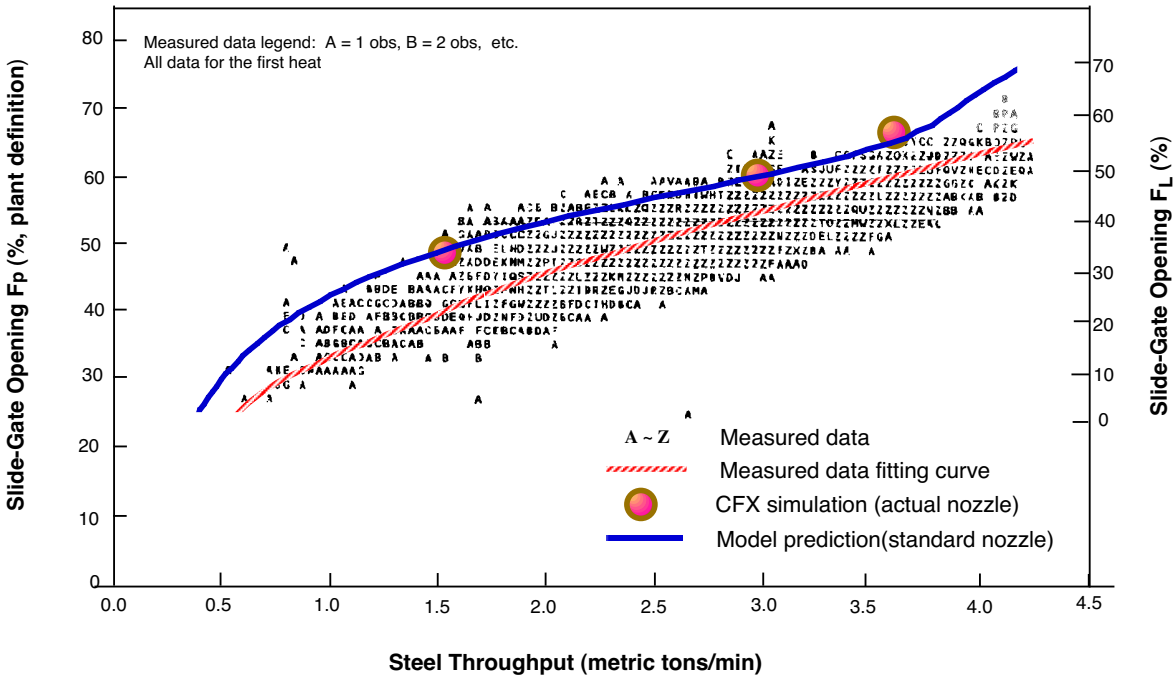

Figure 8 – Comparison of the measurement and the model prediction

Both predictions from the inverse model and CFX simulation match the larger extreme of the range of measured gate opening percentage for a given steel throughput. The decreased gate opening often experienced in the plant is likely due to the following reasons:

- Rounded edge geometry likely found in the plant nozzles may cause smaller pressure drop than the sharp edge in new or simulated nozzles [9], thus need less opening to achieve the same flow.
- Less argon flow in the plant (7~10 SLPM vs. 10 SLPM), needs smaller opening to accommodate the same liquid flow.
- The initial clogging experienced even during the first heat may reduce the gate opening required for a given throughput. This is because, before it starts to restrict the flow channel, the streamlining effect of the initial clogging has been reported to reduce the overall pressure loss [9].

Observations and discussions

The following practical observations can be made from examination of Figure 7:

- Higher casting speed can be achieved by a deeper tundish bath depth (constant gate opening) or larger gate opening (constant bath depth), for a given nozzle geometry and gas flow rate.
- To maintain a constant casting speed, a drop of tundish bath depth must be compensated by increasing the gate opening.
- Casting speed is more sensitive to a change in bath depth at low casting speed than at high casting speed for a given gate opening. This is shown by the flatter slope (dH_T/dV_C) in the low casting speed region of Figure 7(A). Thus, a small change in bath depth causes a larger change in casting speed at low casting speed than it does at high casting speed.
- Casting speed is more sensitive to a bath depth change at large gate opening than at small gate opening (as shown by the steeper slope (dH_T/dV_C) for smaller gate opening in Figure 7(A)).
- To maintain a constant low casting speed, a larger change in gate opening is needed to compensate for small changes in bath depth than maintaining a constant high casting speed

This is as shown by the flatter slope (dH_T/dF_L) in Figure 7(B) at low casting speed. Casting speed is more sensitive to gate opening when maintaining a high casting speed.

- For a fixed tundish bath depth, increasing argon injection will slightly slow down the casting speed (shown in Figure 7(F)) unless the gate opening increases to compensate. This is mainly due to the extra resistance to steel flow due to the space taken up in the nozzle by the buoyant argon gas.
- To maintain constant casting speed while more argon is injected, either gate opening or bath depth needs to increase to accommodate the added gas.
- The theoretical casting speed can be calculated from Equation (26) or directly read from the Figure 7(D) for given tundish bath depth, gate opening, and argon injection flow rate Q_G=5SLPM.
- For a fixed tundish bath depth, casting speed is the most sensitive to gate opening changes at very large openings (F_L>90%) and in the intermediate range of gate opening (F_L=40%~60%). This is shown by the steeper slope (dV_C/dF_L) in Figure 7(D). The intermediate range is most often used in practice.
- Figure 7(D, E and F) appears to show that at very low tundish liquid level (H_T=0.4m), the casting speed drops below zero (as reflected in negative or imaginary roots of Equation (26)) for small gate opening and large argon flow rate. This is due to the fact that the volume fraction of argon injection becomes abnormally high as the casting speed close to zero, so the flow is very buoyant and the small liquid head in tundish cannot overcome the buoyancy and maintain a downward flow.

Conclusions

The two-phase turbulent flow of liquid steel and argon bubbles in a slide-gate nozzle can be simulated with a three-dimensional finite difference model. Model predictions agree both qualitatively and quantitatively with the measurements conducted using PIV (Particle Image Velocimetry) on a 0.4-scale water model in this paper. Flow through a typical nozzle with 90° slide-gate orientation has been simulated with the model to investigate the effects of various casting process variables and their relationship. A model describing the relationship among those process variables, based on Bernoulli's Equation and advanced curve fitting of the multiple variable numerical results, has been developed and applied to convert the numerical modeling results to present trends that correspond with real-life operation conditions. With this inverse model, the theoretical steel flow rate through the nozzle at specific operation conditions can be predicted and clogging condition can be known by comparing the measured steel flow rate to the predicted value under the same operation condition.

Acknowledgments

The authors wish to thank the National Science Foundation (Grant #DMI-98-00274) and the Continuous Casting Consortium at UIUC, including Allegheny Ludlum, (Brackenridge, PA), Armco Inc. (Middletown, OH), Columbus Stainless (South Africa), Inland Steel Corp. (East Chicago, IN), LTV Steel (Cleveland, OH), and Stollberg, Inc., (Niagara Falls, NY) for their continued support of our research, AEA technology for use of the CFX4.2 package and the National Center for Supercomputing Applications (NCSA) at the UIUC for computing time. Additional thanks are extended to technicians at LTV Steel for help with the PIV measurements.

Reference

1. D.E. Hershey, "Turbulent Flow of Molten Steel through Submerged Bifurcated Nozzles in the Continuous Casting Process" (MS Thesis, University of Illinois at Urbana-Champaign, 1992).
2. D. Hershey, B.G. Thomas and F.M. Najjar, "Turbulent Flow through Bifurcated Nozzles," International Journal for Numerical Methods in Fluids 17 (1) (1993), 23-47.
3. F.D. Najjar, "Finite-Element Modelling of Turbulent Fluid Flow and Heat Transfer Through Bifurcated Nozzles in Continuous Steel Slab Casters" (MS Thesis, University of Illinois at Urbana-Champaign, 1990).
4. F.M. Najjar, B.G. Thomas and D. Hershey, "Numerical Study of Steady Turbulent Flow through Bifurcated Nozzles in Continuous Casting," Metallurgical Transactions B, 26B (4) (1995), 749-765.
5. K.G. Rackers and B.G. Thomas, "Clogging in continuous casting nozzles" (Paper presented at SteelMaking Conference Proceedings, 1995), 723-734.

6. B.E. Launder and S.D. B., Mathematical Models of Turbulence, (London: Academic Press, 1972).
7. B.E. Launder and S.D. B., "Numerical computation of turbulrnt flows," (1974),
8. AEA Technology, "CFX4.2 Solver-User's mannual" 1997
9. B.G. Thomas, "Mathematical Models of Continuous Casting of Steel Slabs" (Annual Report, Continuous Casting Consortium, University of Illinois at Urbana-Champaign) 1998).
10. Y.H. Wang, "3-D mathematical model simulation on the tundish gate and its effect in the continuous casting mold" (Paper presented at 10th Process Technology Conference, Toronto, Ontario, Canada, 1992, Iron and Steel Society, Inc.), 75.
11. B.G. Thomas, "Mathematical Models of Continuous Casting of Steel Slabs" (Annual Report, Continuous Casting Consortium, University of Illinois at Urbana-Champaign, 1999).
12. B.G. Thomas, X. Huang and R.C. Sussman, "Simulation of Argon Gas Flow Effects in a Continuous Slab Caster," Metallurgical Transactions B, 25B (4)(1994), 527-547.
13. R. Gass, Private communication, Inland Steel, 1998.